AGU ADVANCING EARTH AND SPACE SCIENCES

Geophysical Research Letters

RESEARCH LETTER
10.1029/2024GL112604

Lithospheric Thinning of the Northeastern Arabian Margin Revealed by Matrix-Free Teleseismic Traveltime Tomography

Gaoshan Guo[1], Haiqiang Lan[1,2], Ling Chen[1,2], Lingkai Meng[1,2], and José Badal[3]

[1]State Key Laboratory of Lithospheric and Environment Coevolution, Institute of Geology and Geophysics, Chinese Academy of Sciences, Beijing, China, [2]College of Earth and Planetary Sciences, University of Chinese Academy of Sciences, Beijing, China, [3]Physics of the Earth, Sciences B, University of Zaragoza, Zaragoza, Spain

Abstract The obduction of the Tethys oceanic lithosphere is documented by the Semail ophiolite along the northeastern Arabian continental margin. Although the ophiolite is continuous and of similar age across the region, the eastern and western segments display distinct geological contrasts. To investigate the deep structural mechanisms underlying these surface variations, we applied teleseismic traveltime tomography using an advanced eikonal solver and a matrix-free adjoint-state approach on data from a dense seismic array. Our 3D upper mantle P-wave model reveals a significant velocity contrast, with positive anomalies in the west and negative anomalies in the east, separated by a prominent fault zone. We propose that the continental lithosphere beneath northeastern Arabia underwent thinning during the Permian breakup of Pangaea. This pre-obduction lithospheric segmentation likely influenced the subduction dynamics associated with the ophiolite obduction process. Additionally, early Cenozoic thermal activity may have further amplified lithospheric thinning, contributing to the observed structural variations.

Plain Language Summary The passive continental margin of northeastern Arabia documents the Late-Cretaceous thrusting process, capturing the obduction of Tethys oceanic lithosphere onto the Arabian continental margin. Despite its significance, geophysical investigations in this region have been notably limited, leading to a considerable gap in our understanding of the regional deep tectonic structure for decades. In particular, high-resolution seismic images of the mantle structure have been absent, which is critical for interpreting tectonic processes and their manifestations on the Earth's surface. To address this issue, we processed a database of teleseismic traveltimes recorded by a newly accessible dense seismic array deployed in the Oman Mountains, utilizing a novel teleseismic traveltime tomography method to successfully image the upper mantle structure. The resulting model provides new seismic evidence for the possible thinning of a cold and stable lithosphere beneath the northeastern Arabian margin.

Key Points:

- The upper mantle structure of northeastern Arabia is imaged using matrix-free teleseismic traveltime tomography to a dense seismic array
- A sharp P-velocity transition is observed at the upper mantle, shifting from a positive anomaly in the west to a negative one in the east
- The lithospheric mantle in this area may been thinned during the Permian rifting of Pangaea and further eroded by Cenozoic thermal activity

Supporting Information:

Supporting Information may be found in the online version of this article.

Correspondence to:

H. Lan,
lanhq@mail.iggcas.ac.cn

Citation:

Guo, G., Lan, H., Chen, L., Meng, L., & Badal, J. (2025). Lithospheric thinning of the northeastern Arabian margin revealed by matrix-free teleseismic traveltime tomography. *Geophysical Research Letters*, *52*, e2024GL112604. https://doi.org/10.1029/2024GL112604

Received 28 SEP 2024
Accepted 31 JAN 2025

Author Contributions:

Conceptualization: Gaoshan Guo
Formal analysis: Gaoshan Guo, Ling Chen, Lingkai Meng
Funding acquisition: Haiqiang Lan, Ling Chen
Investigation: Gaoshan Guo, Lingkai Meng
Methodology: Gaoshan Guo, Haiqiang Lan
Project administration: Haiqiang Lan, Ling Chen
Software: Gaoshan Guo
Supervision: Haiqiang Lan, Ling Chen
Validation: Gaoshan Guo

1. Introduction

The northeastern margin of the Arabian plate is located in the convergence zone between the northward movement of the Arabian plate and the Eurasian plate (Figure 1a). This convergence led to the thrusting of the Tethys oceanic lithosphere in the Late Cretaceous on the Arabian continental margin. Obducted oceanic rocks are recognized as the Semail ophiolite in northeastern Arabia (Searle, 2019) and the largest and best-exposed portion of the oceanic lithosphere on land. Over the decades, different mappings have been carried out: geological (Nicolas & Boudier, 1995), structural (Coleman, 1981; Searle & Cox, 1999), petrological (Kelemen et al., 1997), geochronological (Hacker et al., 1996), and also geophysical explorations of the crust (Al-Lazki et al., 2002; Ali et al., 2020; Levell et al., 2021; Pilia et al., 2021), which have collectively enhanced our understanding of the surface geology and tectonic evolution of the ophiolites.

The tectonic evolution of the Arabian passive margin can be divided into three periods with the well-known Semial ophiolite obduction: pre-obduction (before 110 Ma), Semail obduction (95–75 Ma), and post-obduction process (after 75 Ma) (Weidle et al., 2023). The pre-obduction process is primarily characterized by the Neoproterozoic assembly including NNE-striking terranes along major boundaries parallel to the western Jabal Akhdar Zone (WJAZ), Semail Gap Fault Zone (SGFZ) and Ibera Zone (Stern & Johnson, 2010) (Figure 1a). Subsequently, the breakup of Pangaea during the Permian-Triassic separated Arabia from the continental blocks of western Cimmeria through the evolution of the Neo-Tethys Ocean in the north and Greater India through the

Writing – original draft: Gaoshan Guo, Ling Chen, Lingkai Meng, José Badal
Writing – review & editing: Gaoshan Guo, Haiqiang Lan, Ling Chen, José Badal

evolution of the Batain Basin in the east (Schreurs & Immenhauser, 1999) (Figure 1b). During this rifting event, substantial volumes of Permian mafic rocks were preserved in the Saih Hatat Dome (SHD), eastern of the SGFZ, and only sparse occurrences in the Jabal Akhdar Dome (JAD) (Chauvet et al., 2009) (Figure 1a). Then, SW-directed obduction of Semail Ophiolite was initialized by intraoceanic subduction, followed by short-lived continental subduction (Yamato et al., 2007). Evidence of the continental subduction is recorded in metamorphic rocks, with burial depths 80 km in SHD (Searle et al., 2004) and <25 km in JAD (Grobe et al., 2019). Lastly, the post-obduction phase is marked by the uplift of the Oman Mountains, which may have resulted from late Eocene extension (Scharf et al., 2019) possibly associated with the thermal activity during that period (Gaina et al., 2015; Weidle et al., 2023). This tectonic extension may have facilitated the intrusion of basanites (indicated in Figure 1a), which contain mantle xenoliths that suggest a shallow lithospheric base (Nasir et al., 2006). Throughout the long-term tectonic evolution, the Semail ophiolite has remained relatively continuous and exhibits a consistent age along the strike (Rioux et al., 2013). In contrast, two large tectonic windows, JAD and SHD, exhibit significant geological differences, as summarized in Table 1 of Ninkabou et al. (2021). However, what causes the differential distribution of these surface features? The potential deep mechanics responsible for these variations in surface characteristics remain ambiguous.

Previous large-scale seismic tomography studies (Celli et al., 2020; Koulakov et al., 2016; Pilia et al., 2020; Priestley et al., 2012; van Herwaarden et al., 2023), gravity anomaly (Ravaut et al., 1997), magnetic modeling (Geng et al., 2022) and thermochemical modeling (Fullea et al., 2021) have provided crude information on the continental lithospheric thickness and Moho depth of the northeastern Arabian margin. However, these observations lack the necessary density to generate high-resolution images of this complex region. The deployment of a dense seismic network, named COOL (Crust of the Oman Ophiolite and its Lithosphere) project (Weidle et al., 2013) (Figure 1c) offers an unprecedented opportunity to improve our understanding of the current configuration of the Oman ophiolite and the underlying continental lithosphere. Using this data set, recent research has delved into the shear velocity structure of the crust using ambient noise tomography (Weidle et al., 2022; Wiesenberg et al., 2022), mapping of the Moho depth by receiver function analysis (Weidle et al., 2022, 2023), exploring anisotropy through shear wave splitting (Komeazi et al., 2024) and investigating seismicity and state of stress from focal mechanisms (Weidle et al., 2025). However, these studies offer little information regarding the upper mantle velocity structure of the target region and limit the understanding of the role of lithosphere structure on the difference of tectonic evolution along SGFZ in northeastern Arabia. Therefore, a high-resolution tomographic image of the upper mantle structure is essential for a comprehensive understanding of the evolution of this area.

To investigate the upper mantle structure beneath the northeastern Arabian margin, we analyze teleseismic P-wave traveltime data collected during the COOL project (Weidle et al., 2013), implemented mainly in the Oman Mountains (Figure 1c). Next, we employ a novel teleseismic traveltime tomography approach to image the upper mantle structure. This method combines an efficient eikonal solver (Zhou et al., 2023) and quasi-Newton optimization with a matrix-free adjoint-state method for the computation of gradient and preconditioner of the cost function (Guo et al., 2022). During the inversion process, a previously obtained crustal structure model (Weidle et al., 2022) allows correction of the crustal effect to refine the images of the upper mantle. The resulting P-wave velocity model provides new evidence for the tectonic processes that possibly reshaped the Arabian continental lithosphere. It also establishes a connection between surface geology and deep structure.

2. Method

Since the pioneering work of Aki et al. (1977), teleseismic tomography has undergone significant advancements, progressing from traveltime tomography (Liu et al., 2018; Rawlinson et al., 2006) to finite-frequency traveltime tomography (Dahlen et al., 2000) and more recently, waveform tomography (Beller et al., 2018; Monteiller et al., 2015; Wang et al., 2022). Among these techniques, waveform tomography is particularly notable for its ability to achieve unprecedented resolution and utilize waveform information provided by teleseismic data. However, its widespread application remains limited due to substantial computational costs and stringent requirements for high-quality seismic data. Currently, the widely used methods remain traveltime tomography and finite-frequency tomography because of their feasibility and low cost, while the improvement of finite-frequency kernels in resolution is limited when good data coverage is available (Tong et al., 2011). Thus, this study still focuses on teleseismic traveltime tomography.

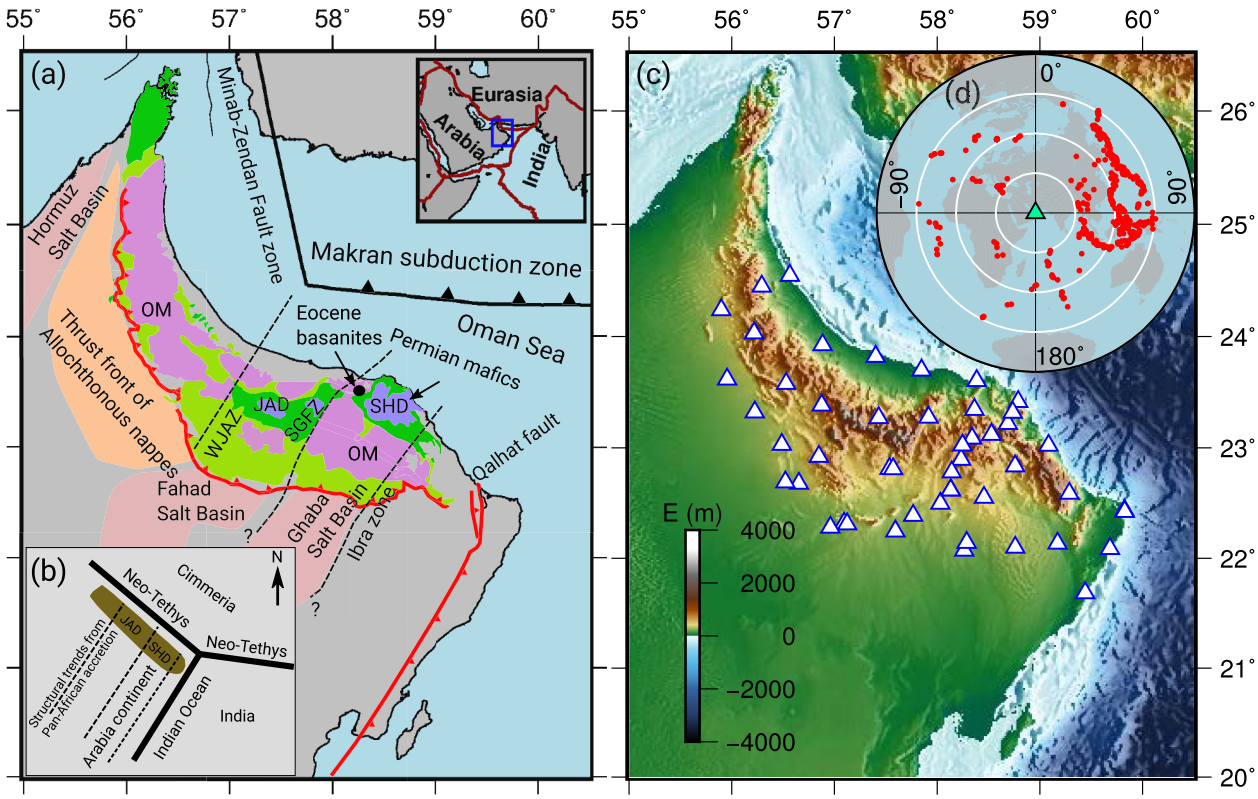

Figure 1. (a) Simplified tectonic map of the northeastern edge of the Arabian plate (Weidle et al., 2022) and location of the study area (delimited by a blue rectangle on the inset map in the upper right corner). OM: Oman Mountains; SGFZ: Semail Gap Fault Zone; WJAZ: Western Jabal Akhdar Zone; JAD: Jabal Akhdar Dome; SHD: Saih Hatat Dome. (b) Plate geometry during the breakup of Pangaea in the Permian (Weidle et al., 2023). (c) Topography and bathymetry of the northeastern Arabian margin. White triangles with blue borders indicate the positions of temporary stations belonging to the COOL network. (d) Location of earthquakes selected for teleseismic tomography on a polar map, where the red dots represent 513 teleseismic earthquakes and the central green triangle indicates the study area.

Classical teleseismic traveltime tomography traditionally relies on ray-tracing and explicit computation of the Frechét matrix (Zhao et al., 1994). In the last decade, eikonal solvers based on the fast marching method (FMM) (Rawlinson & Sambridge, 2004) and the fast sweeping method (FSM) (Lan & Zhang, 2013) have emerged as more robust alternatives for traveltime computation, especially in the case of strongly heterogeneous media. In the context of eikonal-based tomography, ray-paths are subsequently traced to compute the Frechét matrix (Liu et al., 2018, 2019; Rawlinson et al., 2006). To avoid the computation and storage of this matrix, matrix-free traveltime tomography based on the eikonal solver and the adjoint-state method has been proposed (Leung & Qian, 2006). This framework has gained great popularity in the field of exploration seismology due to the adaption to irregular grids, generalization to anisotropic media, and minimal memory requirements for massive seismic data sets (Guo et al., 2022; Sambolian et al., 2019; Tavakoli et al., 2017; Tavakoli F et al., 2019). Recently, this method has also been applied to local (Biondi et al., 2023; Tong, 2021) and teleseismic (Chen et al., 2023) earthquake tomography, even to ambient noise tomography (Hao et al., 2024). Compared to previous studies, our goal is to develop a novel teleseismic traveltime tomography using an advanced eikonal solver (Zhou et al., 2021, 2023), a preconditioned adjoint-state technique (Guo et al., 2022), and a quasi-Newton iterative algorithm for model estimation.

2.1. Efficient Eikonal Solver for Teleseismic Traveltimes

Under the high-frequency approximation, the eikonal equation establishes the relationship of the traveltime T from a source to any points $\mathbf{x}$ of the medium with seismic velocity v,

$$|\nabla T(\mathbf{x})|^2 = 1/v^2(\mathbf{x}), \mathbf{x} \in \Omega \quad \text{and boundary condition} \quad T(\mathbf{x}_s) = f(\mathbf{x}_s), \mathbf{x}_s \in \Gamma, \tag{1}$$

where $\mathbf{x} = (r, \theta, \phi)$ with geocentric distance r, colatitude θ and longitude ϕ in a spherical coordinate system, Ω is the target local model, Γ denotes the bottom of the local model and $f(\mathbf{x}_s)$ represents traveltimes in the bottom using analytical predictions, assuming a spherical symmetry reference model, AK135 (Kennett et al., 1995), beyond the boundaries of the local model. The 3D local model is parameterized with the cubic B-spline function, and the eikonal solver is initialized from $\mathbf{x}_s$ to calculate the traveltimes to the stations. The discretization of the eikonal equation is performed using second-order upwind finite-difference and the locking sweeping method (LSM) (Zhou et al., 2023) as a global scheme to compute teleseismic traveltimes. In comparison with FMM (Rawlinson et al., 2006) and FSM (Chen et al., 2023), LSM exhibits significantly improved computational efficiency (Text S1 in Supporting Information S1).

2.2. Relative Traveltime Residuals

For teleseismic traveltime tomography, the relative traveltime residual $(D_{s,r})$ from the source s to the receiver r is expressed as follows (Rawlinson et al., 2006):

$$D_{s,r} = \left(T_{s,r} - T^{ref}_{s,r}\right) - \frac{1}{N^s_r}\sum_{r=1}^{N^s_r}\left(T_{s,r} - T^{ref}_{s,r}\right), \tag{2}$$

where $T_{s,r}$ and $T^{ref}_{s,r}$ denote absolute traveltimes from the theoretical and reference models, respectively, and N^s_r is the number of observed arrivals for source s, $T_{s,r}$ is sampled at stations from the 3D traveltime field $T_s(\mathbf{x})$ using B-spline interpolation $(B_{s,r})$,

$$T_{s,r} = B_{s,r} T_s(\mathbf{x}). \tag{3}$$

2.3. Adjoint-State Method for Teleseismic Traveltime Tomography

The misfit function for teleseismic traveltime tomography is defined as the least-squares norm of relative traveltime residuals plus the zero-order Tikhonov regularization:

$$\mathcal{J}(\mathbf{v}) = \frac{1}{2}\sum_{s=1}^{N_s}\sum_{r=1}^{N^s_r}\left(\frac{D^*_{s,r} - D_{s,r}(\mathbf{v})}{C^d_{s,r}}\right)^2 + \frac{\epsilon}{2}\sum_{i=1}^{M}\left(\frac{v(x_i) - v(x_i)^{ref}}{C^v_i}\right)^2, \tag{4}$$

where $*$ refers to the observed data, N_s is the number of teleseismic events, C^d is the prior data covariance matrix, $\mathbf{v}^{ref}$ refers to the reference model, M is the number of model parameters, C^v is the prior model covariance matrix, ϵ is the damping factor. This damped least-squares problem can be solved by a gradient-based local optimization scheme. The model update for n^{th} iteration in the vicinity of the model $\mathbf{v}_n$ is given as:

$$\mathbf{v}_{n+1} = \mathbf{v}_n - \alpha_n \mathbf{H}(\mathbf{v}_n)^{-1}\mathbf{g}(\mathbf{v}_n), \tag{5}$$

where step length α_n is estimated using the strong Wolfe condition and the inverse Hessian matrix $\mathbf{H}(\mathbf{v}_n)^{-1}$ is approximated using the preconditioned limited-memory Broyden-Fletcher-Goldfarb-Shanno (L-BFGS) method (Métivier & Brossier, 2016). Here, the gradient $\mathbf{g}(\mathbf{v}_n)$ of the data-fitting term in the cost function is computed with the adjoint-state method (Plessix, 2006) free from the computation of the Fréchet matrix (see the explanation in Text S2 in Supporting Information S1). First, we build the Lagrangian misfit function by augmenting the misfit function Equation 4 with state Equations 1–3 following the strategy of Tavakoli F et al. (2019),

$$\mathcal{L}(\mathbf{v},\mathbf{u},\tilde{\mathbf{u}}) = \mathcal{J}(\mathbf{v},\mathbf{u}) + \frac{1}{2}\sum_{s=1}^{N_s}\left\langle \lambda_s(\mathbf{x})\left(|\nabla T_s(\mathbf{x})|^2 - \frac{1}{v(\mathbf{x})^2}\right)\right\rangle_{\Omega} - \sum_{s=1}^{N_s}\sum_{r=1}^{N_r^s}\zeta_{s,r}\left(D_{s,r} - \left((T_{s,r} - T_{s,r}^{ref}) - \frac{1}{N_r^s}\sum_{r=1}^{N_r^s}(T_{s,r} - T_{s,r}^{ref})\right)\right) - \sum_{s=1}^{N_s}\sum_{r=1}^{N_r^s}\mu_{s,r}(T_{s,r} - B_{s,r}T_s(\mathbf{x})). \quad (6)$$

In this equation, variables $\mathbf{u} = (D_{s,r}, T_{s,r}, T_s)$ and $\tilde{\mathbf{u}} = (\zeta_{s,r}, \mu_{s,r}, \lambda_s)$ encompass both state and adjoint-state variables, respectively. According to the first-order optimization condition, we proceed to enforce $\partial\mathcal{L}/\partial\mathbf{u} = 0$, so that we have the following adjoint-state equation:

$$\nabla\cdot(-\lambda_s(\mathbf{x})\nabla T_s(\mathbf{x})) = \sum_{r=1}^{N_r^s} B_{s,r}^T \frac{D_{s,r}(\mathbf{v}) - D_{s,r}^*}{(C_{s,r}^d)^2}\left(1 - \frac{1}{N_r^s}\right). \quad (7)$$

Similarly, the adjoint-state algorithm combines a local finite difference operator and the FSM to propagate the weighted residuals back to the model (Leung & Qian, 2006). We compute the gradient of the cost function to model parameters with the expression:

$$\mathbf{g} = \frac{\partial\mathcal{J}}{\partial\mathbf{v}} = \frac{\partial\mathcal{L}}{\partial\mathbf{v}} = \sum_{s=1}^{N_s}\frac{\lambda_s(\mathbf{x})}{v^3(\mathbf{x})}. \quad (8)$$

The preconditioner is estimated by solving the same adjoint-state Equation 7 using constant initial conditions (Guo et al., 2022; Zhang et al., 2024). We use this scheme to compensate for uneven ray illumination from teleseismic events to seismic stations (see numerical validation in Text S3 in Supporting Information S1). Additionally, this preconditioner, or approximated diagonal Hessian matrix is a good proxy for the ray density coverage (Zhu et al., 2020).

3. Results

3.1. Data Configuration

Teleseismic waveforms were recorded by 49 temporary seismic stations deployed for the COOL project in operation between November 2013 and February 2016 (Figure 1c). The raw waveforms were processed by removing the instrument response and the mean and linear trend. Next, the data were bandpass filtered with corner frequencies between 0.1 and 2.0 Hz. We specifically chose earthquakes with magnitudes >4.8, ensuring that direct P-waves were recorded by at least four stations at epicentral distances of 30°–90° (Figure 1d). The data set comprises 11,334 direct P-wave relative traveltime residuals obtained from 513 teleseismic events. Most of the earthquakes have back azimuths between 25° and 125° and epicentral distances between 60° and 90°, and originate mainly in the subduction zones of the Western Pacific and Eurasian plates. Teleseismic relative traveltimes were manually picked using stacking correlation and multi-channel cross-correlation (MCCC) methods (Lou et al., 2013; VanDecar & Crosson, 1990). Lateral P-wave velocity variations are directly indicated by azimuthally averaged relative traveltime anomalies ($D_{s,r}^* - D_{s,r}(\mathbf{v})$) at each station before (Figure 2a) and after (Figure 2b) tomographic inversion. The observed differential traveltimes (Figure 2a) already highlight a main characterization of the final model: a negative delay time means a positive velocity anomaly in the western region, while a positive delay time indicates a negative velocity anomaly in the eastern region. The inversion stops after 15 iterations when the misfit reduction is more than 80% (Figure 2d) and final data residuals are significantly minimized and show a Gaussian distribution (Figure 2c) (see Text S4 in Supporting Information S1 for the crust correction and model setting and S5 for the configuration of inversion).

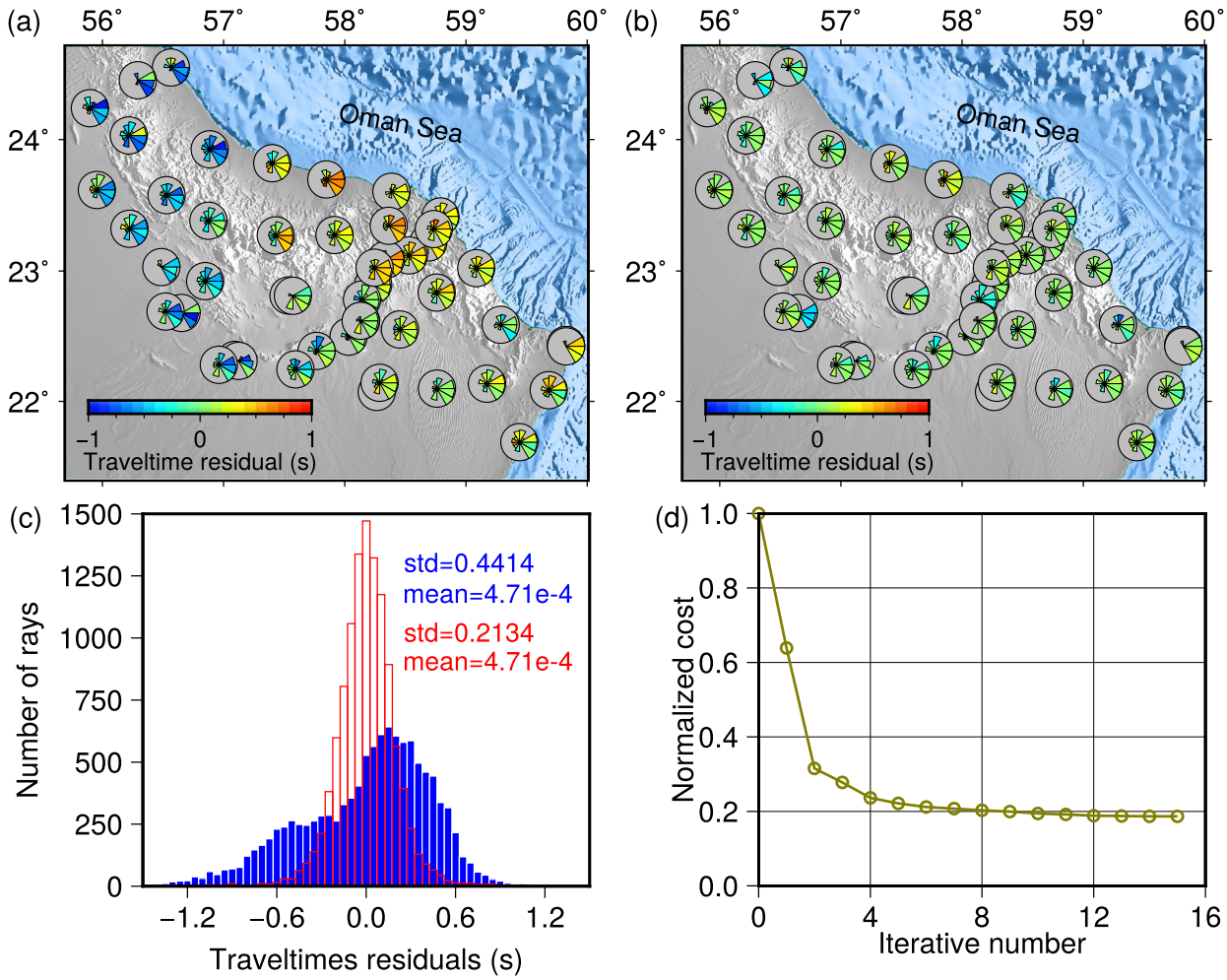

Figure 2. (a and b) Sector diagrams of azimuthally averaged relative traveltime anomalies before (a) and after (b) teleseismic tomographic inversion. Every sector diagram denotes the normalized relative traveltime anomalies in the range of 30° back-azimuth at each station, where the length of the sector represents the number of measurements and the color of the sector is the average of the relative traveltime anomalies (Liang et al., 2016). (c) Histograms of relative traveltime anomalies before (blue) and after (red) tomographic inversion, where the mean and standard deviations of anomalies are shown using the same color as the bars. (d) Convergence curve of the normalized cost function during the inversion process.

3.2. Resolution Assessment

To evaluate the resolution and main characteristics of the final model derived from the data set, we conducted two essential synthetic validations, namely: checkerboard resolution tests (Text S6 in Supporting Information S1) and recovery tests (Text S7 in Supporting Information S1). As shown in Figure S11 in Supporting Information S1, the output checkerboard models exhibit successful retrieval on well-sampled regions, although smearing effects become evident near the periphery of the study region due to limited ray path coverage. The results obtained from the synthetic recovery tests (Figure S12 in Supporting Information S1) confirm the feasibility of resolving low-velocity and high-velocity perturbations similar to those shown in Figure 3. Furthermore, the ray-density from the approximated diagonal Hessian also serves as validation for the illumination of major anomalies (Figure S13 in Supporting Information S1).

3.3. Tomographic Results

Figure 3 shows the P-wave velocity perturbations in percentage ($\delta v_p/v_p$) relative to the reference AK135 model. The color scale is set to ±4% to show a weaker smearing effect. These slices are superimposed by the contour of ray density to indicate the ray illumination (Text S8 in Supporting Information S1). For comparison, Figure S14 in Supporting Information S1 displays the results with a color scale of ±2% to highlight the weak anomalies in the

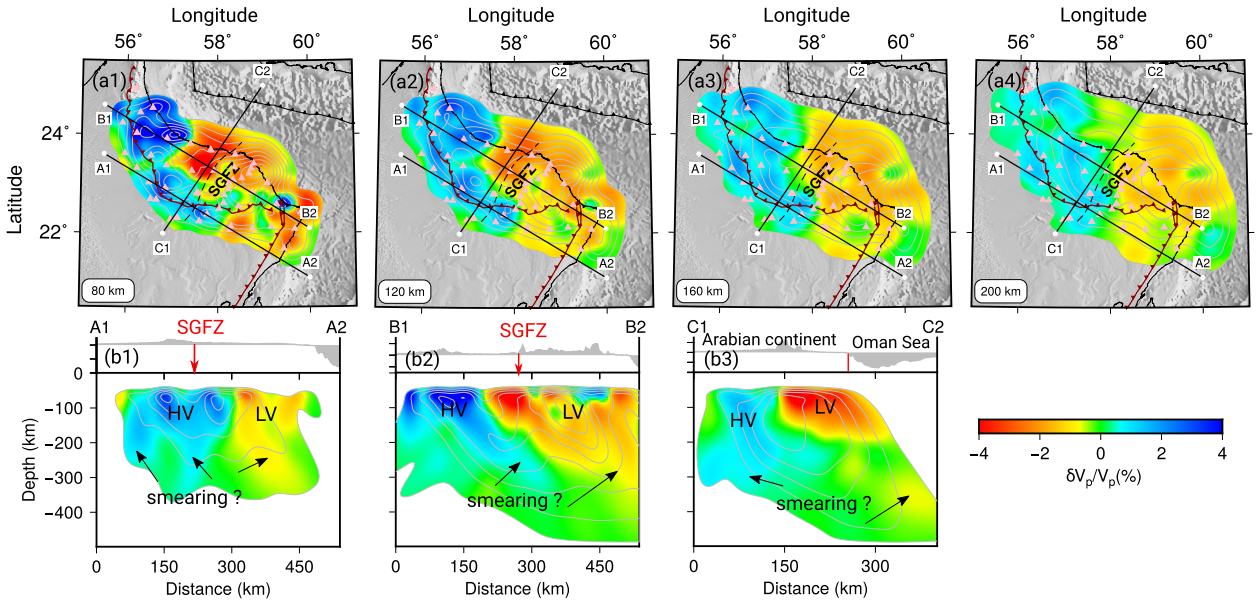

Figure 3. Velocity perturbations in percentage $\delta v_p/v_p$ beneath northeastern Arabia revealed by teleseismic traveltime tomography. (a1-4) Horizontal P-wave velocity slices showing velocity variations at depths from 80 to 200 km. (b1-3) West-to-east (b1-b2) and south-to-north (b3) vertical sections of P-wave velocity. The locations of these profiles (A1-A2, B1-B2, and C2-C2) are indicated in panel (a1-4). HV means high velocity and LV means low velocity. The velocity slices are muted according to the 0.2 contour of the approximated diagonal Hessian (ray density) in Figure S13 in Supporting Information S1. The contours of the approximated diagonal Hessian are superimposed on the velocity patterns to indicate the ray illumination. The contour interval is 0.2, with a minimum contour value of 0.2. Pink triangles indicate the positions of temporary stations of the COOL array. The red lines denote the thrust fronts, which are the same as in Figure 1a. The SGFZ is represented by a black dotted line.

deeper regions (Text S9 in Supporting Information S1). Based on the results of the checkerboard and recovery tests, we believe that the resolution for depth above 200 km is optimal, so we present four horizontal slices at depths of 80, 120, 160, and 200 km (Figures 3a1–3a4). An initial observation is the existence of significant high-velocity anomalies in the west, in contrast to low-velocity zones in the east of the study area. As the depth increases, the velocity contrast boundary rotates from the northwest (at approximately <160 km depth) toward the north (within the range of 160–200 km depth) and further toward the northeast (at approximately >200 km depth with poor resolution). For the depth above 200 km, there is a concentrated high-velocity (HV) anomaly that persists at deeper levels, extending widely to the north and east. At the same time, a low-velocity (LV) anomaly concentrates along the eastern coastline of the target zone. This pattern suggests clear segmentation and heterogeneity of the northeastern Arabian margin at the upper mantle scale. For further illustration in Figures 3b1–3b3, we include two west-to-east vertical slices and one south-to-north vertical slice extracted from the P-wave velocity model. Nevertheless, due to the possible smearing effects in the NNE direction of the ray paths, the dipping structure between high-velocity and low-velocity anomalies has not yet been resolved by teleseismic traveltime tomography unequivocally. Addressing this limitation may require applying the receiver function or tele-FWI to refine the representation of the dipping structure.

4. Discussion and Interpretation

4.1. New Evidence for the Lithospheric Thinning in the Northeastern Arabian Margin

Our interpretation focuses on the first-order characteristics of the velocity pattern above 200 km depth with good resolution. The western section of the Oman Mountains and Oman Sea display significant high-velocity anomalies, which contrast sharply with low-velocities beneath the eastern section. This clear velocity transition likely delineates the boundary between the continental and oceanic lithospheres beneath the Oman Sea. The high-velocity structure in the western part of the Oman Mountains and Oman Sea is associated with a cold, thick (about 150–200 km) and mechanically strong Arabian continental lithosphere. In contrast, the eastern section may represent a low-velocity asthenospheric structure underlying a thin lithosphere, indicating the thinning of continental lithosphere beneath the eastern Oman Mountains or oceanic lithosphere beneath the Oman Sea,

10.1029/2024GL112604

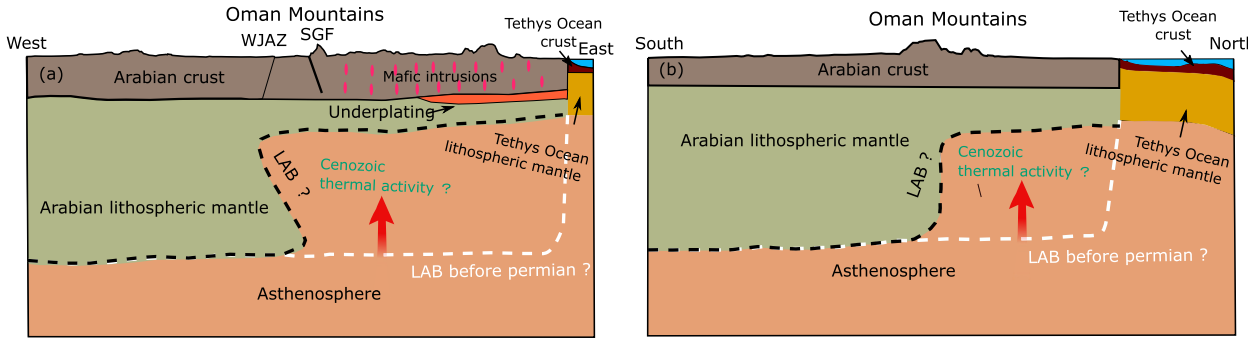

Figure 4. Schematic illustration showing the thinning of continental lithosphere on the margin of northeastern Arabia. The black dashed lines represent the present-day lithosphere-asthenosphere boundary (LAB) inferred from our tomographic images, while the white dashed lines indicate the possible LAB before the Permian rifting of Pangaea. The red arrows denote possible Cenozoic thermal activity from possible mantle plume. Velocity slices are interpreted for (a) profile B from west to east and (b) profile C from south to north, respectively. Due to the limited illumination of the crust in this study, the interpretation is mainly based on the model of Weidle et al. (2023).

respectively. In the following, our interpretation is focusing on the lithospheric thinning in this region. Notably, the nature of these low-velocity anomalies, including their association with a potential new mantle plume, was discussed in a recent preprint of Pilia et al. (2024), which utilized a larger data set.

The NNE trending contrast has been previously documented by other geophysical investigations. In the COOL project, a high-resolution crustal shear-wave velocity model was obtained using ambient noise tomography (Weidle et al., 2022, 2023). An increase in shear-wave velocity in the lower crust beneath the east of the SGFZ was observed, potentially indicating cooling and contraction following the intrusion of significant amounts of molten mafic material into the crust. Using the same data set, shear wave splitting analysis revealed one-layer anisotropy in the western region, possibly indicative of an old and thick lithospheric mantle, and two-layer anisotropy in the eastern region, suggesting asthenospheric thickening beneath a thinning lithosphere (Komeazi et al., 2024). Furthermore, negative residual gravity anomalies indicate low upper mantle density at the western margin (Kaban et al., 2016). This contrast variation is also somewhat visible along northeastern Arabia (Priestley et al., 2012; van Herwaarden et al., 2023) for large-scale seismic models though with rather poor resolution. Especially, a recent continental-scale African-Arabian shear-wave velocity model further favors the occurrence of widespread lithospheric erosion and thinning during the past 200 Ma (Celli et al., 2020). These independent validations are particularly noteworthy since our inversion study is based solely on teleseismic arrival data. The convergence of these various lines of evidence collectively supports the presence of thinning of the continental lithosphere beneath the northeastern Arabian margin.

4.2. Implications for the Tectonic Evolution of the Northeastern Arabian Margin

Combining our upper mantle velocity model and prior geological and geophysical evidence, we propose a schematic representation of this continental lithospheric thinning beneath the northeastern Arabian margin, as shown in Figure 4. This model serves as a basis to discuss the potential mechanisms and implications of this lithospheric thinning for the tectonic evolution of this region, as reviewed in the introduction.

The main tectonic event before the Ophiolite obduction is the Late Proterozoic Pan-African plate assembly and Permian Pangaea rifting and breakup. From the shear-wave velocity model, Weidle et al. (2023) suggested that crustal segmentation along the main NNE boundary, including WJAZ, SGFZ, and Ibra zone, likely was established during the Pan-African orogeny and the high-velocity in the lower crust beneath the eastern SGFZ may reflect Permian mafic intrusions. Building on this perspective, we propose that the low-velocity anomaly in the upper mental scale may result from lithospheric thinning and upwelling of asthenospheric material (Xu & Zhao, 2009) during the rifting of Pangaea in the Permian (Figure 1a). Several geological investigations support the hypothesis of lithospheric thinning along the northeastern Arabian margin during the Middle-Permian rifting. Paleomagnetic data (Besse et al., 1998) indicates that the opening of Neo-Tethys occurred during the Permian, situated between the Cimmerian fragments in the north and the Arabian margin in the south (Figure 1b). The breakup of Pangaea that began in the mid-Permian might have thinned the lithosphere, particularly southeast of the SGFZ. The presence of abundant Permian mafic rocks within the Arabian margin of the SHD has been

attributed to Permian rifting (Chauvet et al., 2009), whereas the JAD appears to have been minimally impacted by mafic intrusions (Figure 1a). The spatial distribution of Permian mafic rocks further supports the view that the SGFZ may have been an active boundary during rifting (Ninkabou et al., 2021; Scharf et al., 2019).

The Semail Ophiolite, formed during the obduction process, appears to be roughly continuous and unaffected by the SGFZ, with similar ages observed along its strike (Rioux et al., 2013). This continuity suggests that the obduction process might have had minimal impact on the upper mantle structure beneath the northeastern Arabian margin. However, pre-obduction lithospheric thinning is likely linked to obduction-related continental subduction. Evidence for the depth of continental subduction is provided by high-pressure rock units exhumed after a potential slab break-off event (Searle et al., 2004). For instance, metamorphic rocks in the SHD, with burial depths of approximately 80 km, are situated at the same structural level as the mildly metamorphosed rocks of the JAD with burial depths of less than 25 km (Grobe et al., 2019; Searle et al., 2004). Furthermore, the denser distribution of normal faults on the eastern side of the SGFZ compared to the JAD indicates more significant exhumation processes (Agard et al., 2010). These observations suggest different amounts of subducted continental materials between the SHD and JAD (Ninkabou et al., 2021). We propose that pre-obduction lithospheric thinning may have facilitated greater continental subduction on the SHD side. Additionally, a potential break-off of the subducted slabs may have influenced the lithospheric structure but is worth more focused research in future.

During the post-obduction period, the lithosphere in this region may have experienced further erosion due to thermal activity in the early Cenozoic. This interpretation aligns with evidence of late Eocene lithospheric extension, as indicated by lower crustal azimuthal anisotropy (Weidle et al., 2023) and offshore seismic stratigraphy (Ninkabou et al., 2021). Geologically, the mantle xenoliths found in basanite rocks in coastal areas of the eastern SGFZ (Figure 1a) support a thinned lithosphere (about 80 km) at that period. Thermal thinning could also explain the late Eocene uplift of the Oman Mountains (Scharf et al., 2019). Weidle et al. (2023) propose that during the early Cenozoic, the eastern Arabian plate was positioned near the present-day Afar triple junction (Gaina et al., 2015). Hot material from the Afar plume likely spread outward, thinning the lithosphere through partial melting and thermal erosion of the lithospheric basement. Additionally, lithospheric delamination driven by small-scale convection (Xi et al., 2024) might have further modified the lithospheric structure along the Arabian continental margin. All these processes could contribute to mantle and lithospheric alterations, though additional observations are required to validate these hypotheses fully.

5. Conclusions

We have developed a new 3D P-wave velocity model for the upper mantle beneath the northeastern Arabian margin using newly available seismological data and a novel form of teleseismic traveltime tomography. The results reveal two column-shaped anomalies: a high-velocity anomaly in the western part and a low-velocity anomaly in the eastern part. These findings may suggest modification and thinning of the cold, thick Arabian continental lithosphere during the Permian rifting of Pangaea. This pre-obduction lithospheric segmentation may have influenced the subduction dynamics during the ophiolite obduction process and the amounts of subducted continental materials. Additionally, potential thermal erosion during the early Cenozoic may have further modified the already thinned lithosphere. To better understand the mechanisms behind this lithospheric thinning, we aim to refine the deeper structures by integrating other data sets provided by recently deployed seismic arrays spanning the Zagros-Makran-Oman collision zone.

Data Availability Statement

The event catalog and all seismic waveforms of the COOL project recorded by network 5H were downloaded from GEOFON (http://eida.gfz-potsdam.de/webdc3/). The following software packages were used: AIMBAT (https://github.com/pysmo/aimbat) for picking teleseismic traveltimes, ObsPy (https://github.com/obspy/obspy) for data processing, and GMT (https://www.generic-mapping-tools.org) for data visualization. The 3D crustal shear-wave velocity model of the Oman Mountains was downloaded from IRIS (http://ds.iris.edu/ds/products/emc-orla2022). The teleseismic traveltime tomography package is accessible from the WDC for Geophysics in Beijing (https://doi.org/10.12197/2024GA020).

Acknowledgments
We thank Editor Prof. Daoyuan Sun for managing the review process of this manuscript and the associate editor and three anonymous reviewers for their constructive comments. We express our gratitude to Prof. Christian Weidle for providing us with unrestricted access to the COOL data set and Prof. Nicholas Rawlinson for making the FMTT code (https://iearth.edu.au/codes/FMTT/) freely accessible. Special thanks to Xiaofeng Liang for data processing, Hao Hu for using ObsPy, Xuelei Li for the discussion of FMTT, and Naeim Mousavi and Xusong Yang for the interpretation. This research was supported by the National Key R&D Program of China (2023YFF0803500) and the Strategic Priority Program (B) of the Chinese Academy of Sciences (XDB24000000). Gaoshan Guo started this study with a master's study at IGGCAS and benefited from the PhD training at CNRS-GEOAZUR to use the SEISCOPE optimization toolbox.

References

Agard, P., Searle, M. P., Alsop, G. I., & Dubacq, B. (2010). Crustal stacking and expulsion tectonics during continental subduction: P-T deformation constraints from Oman. *Tectonics*, *29*(5), TC5018. https://doi.org/10.1029/2010TC002669

Aki, K., Christoffersson, A., & Husebye, E. S. (1977). Determination of the three-dimensional seismic structure of the lithosphere. *Journal of Geophysical Research*, *82*(2), 277–296. https://doi.org/10.1029/JB082i002p00277

Ali, M., Watts, A., Searle, M., Keats, B., Pilia, S., & Ambrose, T. (2020). Geophysical imaging of ophiolite structure in the United Arab Emirates. *Nature Communications*, *11*(1), 2671. https://doi.org/10.1038/s41467-020-16521-0

Al-Lazki, A. I., Seber, D., Sandvol, E., & Barazangi, M. (2002). A crustal transect across the Oman Mountains on the eastern margin of Arabia. *GeoArabia*, *7*(1), 47–78. https://doi.org/10.2113/geoarabia070147

Beller, S., Monteiller, V., Operto, S., Nolet, G., Paul, A., & Zhao, L. (2018). Lithospheric architecture of the south-western alps revealed by multi-parameter teleseismic full-waveform inversion. *Geophysical Journal International*, *212*(2), 1369–1388. https://doi.org/10.1093/gji/ggx216

Besse, J., Torcq, F., Gallet, Y., Ricou, L., Krystyn, L., & Saidi, A. (1998). Late Permian to Late Triassic palaeomagnetic data from Iran: Constraints on the migration of the Iranian block through the Tethyan Ocean and initial destruction of Pangaea. *Geophysical Journal International*, *135*(1), 77–92. https://doi.org/10.1046/j.1365-246X.1998.00603.x

Biondi, E., Zhu, W., Li, J., Williams, E. F., & Zhan, Z. (2023). An upper-crust lid over the Long Valley magma chamber. *Science Advances*, *9*(42), eadi9878. https://doi.org/10.1126/sciadv.adi9878

Celli, N. L., Lebedev, S., Schaeffer, A. J., & Gaina, C. (2020). African cratonic lithosphere carved by mantle plumes. *Nature Communications*, *11*(1), 92. https://doi.org/10.1038/s41467-019-13871-2

Chauvet, F., Dumont, T., & Basile, C. (2009). Structures and timing of Permian rifting in the central Oman Mountains (Saih Hatat). *Tectonophysics*, *475*(3–4), 563–574. https://doi.org/10.1016/j.tecto.2009.07.008

Chen, J., Wu, S., Xu, M., Nagaso, M., Yao, J., Wang, K., et al. (2023). Adjoint-state teleseismic traveltime tomography: Method and application to Thailand in Indochina Peninsula. *Journal of Geophysical Research: Solid Earth*, *128*(12), e2023JB027348. https://doi.org/10.1029/2023JB027348

Coleman, R. G. (1981). Tectonic setting for ophiolite obduction in Oman. *Journal of Geophysical Research*, *86*(B4), 2497–2508. https://doi.org/10.1029/JB086iB04p02497

Dahlen, F. A., Hung, S.-H., & Nolet, G. (2000). Fréchet kernels for finite-frequency traveltimes—I. Theory. *Geophysical Journal International*, *141*(1), 157–174. https://doi.org/10.1046/j.1365-246X.2000.00070.x

Fullea, J., Lebedev, S., Martinec, Z., & Celli, N. (2021). Winterc-g: Mapping the upper mantle thermochemical heterogeneity from coupled geophysical–petrological inversion of seismic waveforms, heat flow, surface elevation and gravity satellite data. *Geophysical Journal International*, *226*(1), 146–191. https://doi.org/10.1093/gji/ggab094

Gaina, C., van Hinsbergen, D. J. J., & Spakman, W. (2015). Tectonic interactions between India and Arabia since the Jurassic reconstructed from marine geophysics, ophiolite geology, and seismic tomography. *Tectonics*, *34*(5), 875–906. https://doi.org/10.1002/2014TC003780

Geng, M., Ali, M. Y., Derek Fairhead, J., Pilia, S., Bouzidi, Y., & Barkat, B. (2022). Crustal structure of the United Arab Emirates and northern Oman Mountains from constrained 3D inversion of gravity and magnetic data: The Moho and basement surfaces. *Journal of Asian Earth Sciences*, *231*, 105223. https://doi.org/10.1016/j.jseaes.2022.105223

Grobe, A., Von Hagke, C., Littke, R., Dunkl, I., Wübbeler, F., Muchez, P., & Urai, J. L. (2019). Tectono-thermal evolution of Oman's Mesozoic passive continental margin under the obducting Semail Ophiolite: A case study of Jebel Akhdar, Oman. *Solid Earth*, *10*(1), 149–175. https://doi.org/10.5194/se-10-149-2019

Guo, G., Lan, H., Zhou, X., Liu, Y., Waheed, U. B., & Chen, J. (2022). Topography-dependent eikonal tomography based on the fast-sweeping scheme and the adjoint-state technique. *Geophysics*, *87*(2), U29–U41. https://doi.org/10.1190/geo2021-0116.1

Hacker, B., Mosenfelder, J., & Gnos, E. (1996). Rapid emplacement of the Oman ophiolite: Thermal and geochronologic constraints. *Tectonics*, *15*(6), 1230–1247. https://doi.org/10.1029/96TC01973

Hao, S., Chen, J., Xu, M., & Tong, P. (2024). Topography-incorporated adjoint-state surface wave traveltime tomography: Method and a case study in Hawaii. *Journal of Geophysical Research: Solid Earth*, *129*(1), e2023JB027454. https://doi.org/10.1029/2023JB027454

Kaban, M. K., El Khrepy, S., Al-Arifi, N., Tesauro, M., & Stolk, W. (2016). Three-dimensional density model of the upper mantle in the Middle East: Interaction of diverse tectonic processes. *Journal of Geophysical Research: Solid Earth*, *121*(7), 5349–5364. https://doi.org/10.1002/2015JB012755

Kelemen, P. B., Koga, K., & Shimizu, N. (1997). Geochemistry of gabbro sills in the crust-mantle transition zone of the Oman ophiolite: Implications for the origin of the oceanic lower crust. *Earth and Planetary Science Letters*, *146*(3–4), 475–488. https://doi.org/10.1016/S0012-821X(96)00235-X

Kennett, B. L. N., Engdahl, E. R., & Buland, R. (1995). Constraints on seismic velocities in the Earth from travel times. *Geophysical Journal International*, *122*(1), 108–124. https://doi.org/10.1111/j.1365-246X.1995.tb03540.x

Komeazi, A., Kaviani, A., Rümpker, G., Weidle, C., & Meier, T. (2024). Discriminating lithospheric and asthenospheric anisotropy beneath Northern Oman: Sharp contrast observed at the Semail Gap Fault Zone. *Journal of Geophysical Research: Solid Earth*, *129*(6), e2023JB028627. https://doi.org/10.1029/2023JB028627

Koulakov, I., Burov, E., Cloetingh, S., El Khrepy, S., Al-Arifi, N., & Bushenkova, N. (2016). Evidence for anomalous mantle upwelling beneath the Arabian Platform from travel time tomography inversion. *Tectonophysics*, *667*, 176–188. https://doi.org/10.1016/j.tecto.2015.11.022

Lan, H., & Zhang, Z. (2013). Topography-dependent eikonal equation and its solver for calculating first-arrival traveltimes with an irregular surface. *Geophysical Journal International*, *193*(2), 1010–1026. https://doi.org/10.1093/gji/ggt036

Leung, S., & Qian, J. (2006). An adjoint state method for three-dimensional transmission traveltime tomography using first-arrivals. *Communications in Mathematical Sciences*, *4*(1), 249–266. https://doi.org/10.4310/CMS.2006.v4.n1.a10

Levell, B., Searle, M., White, A., Kedar, L., Droste, H., & Van Steenwinkel, M. (2021). Geological and seismic evidence for the tectonic evolution of the NE Oman continental margin and Gulf of Oman. *Geosphere*, *17*(5), 1472–1493. https://doi.org/10.1130/GES02376.1

Liang, X., Chen, Y., Tian, X., Chen, Y. J., Ni, J., Gallegos, A., et al. (2016). 3D imaging of subducting and fragmenting Indian continental lithosphere beneath southern and central Tibet using body-wave finite-frequency tomography. *Earth and Planetary Science Letters*, *443*, 162–175. https://doi.org/10.1016/j.epsl.2016.03.029

Liu, S., Suardi, I., Yang, D., Wei, S., & Tong, P. (2018). Teleseismic traveltime tomography of Northern Sumatra. *Geophysical Research Letters*, *45*(24), 13231–13239. https://doi.org/10.1029/2018GL078610

Liu, S., Suardi, I., Zheng, M., Yang, D., Huang, X., & Tong, P. (2019). Slab morphology beneath Northern Sumatra revealed by regional and teleseismic traveltime tomography. *Journal of Geophysical Research: Solid Earth*, *124*(10), 10544–10564. https://doi.org/10.1029/2019JB017625

Lou, X., van der Lee, S., & Lloyd, S. (2013). AIMBAT: A Python/Matplotlib tool for measuring teleseismic arrival times. *Seismological Research Letters*, *84*(1), 85–93. https://doi.org/10.1785/0220120033

Métivier, L., & Brossier, R. (2016). The SEISCOPE optimization toolbox: A large-scale nonlinear optimization library based on reverse communication. *Geophysics*, *81*(2), F11–F25. https://doi.org/10.1190/geo2015-0031.1

Monteiller, V., Chevrot, S., Komatitsch, D., & Wang, Y. (2015). Three-dimensional full waveform inversion of short-period teleseismic wavefields based upon the SEM–DSM hybrid method. *Geophysical Journal International*, *202*(2), 811–827. https://doi.org/10.1093/gji/ggv189

Nasir, S., Al-Sayigh, A., Alharthy, A., & Al-Lazki, A. (2006). Geochemistry and petrology of tertiary volcanic rocks and related ultramafic xenoliths from the central and eastern Oman Mountains. *Lithos*, *90*(3), 249–270. https://doi.org/10.1016/j.lithos.2006.03.002

Nicolas, A., & Boudier, F. (1995). Mapping oceanic ridge segments in Oman ophiolite. *Journal of Geophysical Research*, *100*(B4), 6179–6197. https://doi.org/10.1029/94JB01188

Ninkabou, D., Agard, P., Nielsen, C., Smit, J., Gorini, C., Rodriguez, M., et al. (2021). Structure of the offshore obducted Oman margin: Emplacement of Semail Ophiolite and role of tectonic inheritance. *Journal of Geophysical Research: Solid Earth*, *126*(2), 2020JB020187. https://doi.org/10.1029/2020JB020187

Pilia, S., Ali, M. Y., Searle, M. P., Watts, A. B., Lü, C., & Thompson, D. A. (2021). Crustal structure of the UAE-Oman mountain range and Arabian rifted passive margin: New constraints from active and passive seismic methods. *Journal of Geophysical Research: Solid Earth*, *126*(4), e2020JB021374. https://doi.org/10.1029/2020JB021374

Pilia, S., Hu, H., Ali, M. Y., Rawlinson, N., & Ruan, A. (2020). Upper mantle structure of the northeastern Arabian Platform from teleseismic body-wave tomography. *Physics of the Earth and Planetary Interiors*, *307*, 106549. https://doi.org/10.1016/j.pepi.2020.106549

Pilia, S., Iaffaldano, G., Davies, D. R., Sossi, P., Whattam, S., & Hu, H. (2024). Ghost plumes hidden beneath Earth's continents. *Preprint in Research Square*. https://doi.org/10.21203/rs.3.rs-4526590/v1

Plessix, R. E. (2006). A review of the adjoint-state method for computing the gradient of a functional with geophysical applications. *Geophysical Journal International*, *167*(2), 495–503. https://doi.org/10.1111/j.1365-246X.2006.02978.x

Priestley, K., McKenzie, D., Barron, J., Tatar, M., & Debayle, E. (2012). The Zagros core: Deformation of the continental lithospheric mantle. *Geochemistry, Geophysics, Geosystems*, *13*(11). https://doi.org/10.1029/2012GC004435

Ravaut, P., Bayer, R., Hassani, R., Rousset, D., & Al Yahya'ey, A. (1997). Structure and evolution of the northern Oman margin: Gravity and seismic constraints over the Zagros-Makran-Oman collision zone. *Tectonophysics*, *279*(1–4), 253–280. https://doi.org/10.1016/S0040-1951(97)00125-X

Rawlinson, N., Reading, A. M., & Kennett, B. L. N. (2006). Lithospheric structure of Tasmania from a novel form of teleseismic tomography. *Journal of Geophysical Research*, *111*(B2), B02301. https://doi.org/10.1029/2005JB003803

Rawlinson, N., & Sambridge, M. (2004). Wave front evolution in strongly heteregeneous layered media using the fast marching. *Geophysical Journal International*, *156*(3), 631–647. https://doi.org/10.1111/j.1365-246X.2004.02153.x

Rioux, M., Bowring, S., Kelemen, P., Gordon, S., Miller, R., & Dudás, F. (2013). Tectonic development of the Samail ophiolite: High-precision U-Pb zircon geochronology and Sm-Nd isotopic constraints on crustal growth and emplacement. *Journal of Geophysical Research: Solid Earth*, *118*(5), 2085–2101. https://doi.org/10.1002/jgrb.50139

Sambolian, S., Operto, S., Ribodetti, A., Tavakoli, B., & Virieux, J. (2019). Parsimonious slope tomography based on eikonal solvers and the adjoint-state method. *Geophysical Journal International*, *218*(1), 456–478. https://doi.org/10.1093/gji/ggz150

Scharf, A., Mattern, F., Moraetis, D., Callegari, I., & Weidle, C. (2019). Postobductional kinematic evolution and geomorphology of a major regional structure—The Semail Gap Fault Zone (Oman Mountains). *Tectonics*, *38*(8), 2756–2778. https://doi.org/10.1029/2019TC005588

Schreurs, G., & Immenhauser, A. (1999). West-northwest directed obduction of the Batain Group on the eastern Oman continental margin at the Cretaceous-Tertiary boundary. *Tectonics*, *18*(1), 148–160. https://doi.org/10.1029/1998TC900020

Searle, M. (2019). *Geology of the Oman Mountains, eastern Arabia*. Springer.

Searle, M., & Cox, J. (1999). Tectonic setting, origin, and obduction of the Oman ophiolite. *Geological Society of America Bulletin*, *111*(1), 104–122. https://doi.org/10.1130/0016-7606(1999)111⟨0104:TSOAOO⟩2.3.CO;2

Searle, M., Warren, C., Waters, D., & Parrish, R. (2004). Structural evolution, metamorphism and restoration of the Arabian continental margin, Saih Hatat region, Oman Mountains. *Journal of Structural Geology*, *26*(3), 451–473. https://doi.org/10.1016/j.jsg.2003.08.005

Stern, R. J., & Johnson, P. (2010). Continental lithosphere of the Arabian Plate: A geologic, petrologic, and geophysical synthesis. *Earth-Science Reviews*, *101*(1–2), 29–67. https://doi.org/10.1016/j.earscirev.2010.01.002

Tavakoli, B., Operto, S., Ribodetti, A., & Virieux, J. (2017). Slope tomography based on eikonal solvers and the adjoint-state method. *Geophysical Journal International*, *209*(3), 1629–1647. https://doi.org/10.1093/gji/ggx111

Tavakoli F, B., Operto, S., Ribodetti, A., & Virieux, J. (2019). Matrix-free anisotropic slope tomography: Theory and application. *Geophysics*, *84*(1), R35–R57. https://doi.org/10.1190/geo2018-0112.1

Tong, P. (2021). Adjoint-State traveltime tomography: Eikonal equation-based methods and application to the Anza Area in Southern California. *Journal of Geophysical Research: Solid Earth*, *126*(5), e2021JB021818. https://doi.org/10.1029/2021JB021818

Tong, P., Zhao, D., & Yang, D. (2011). Tomography of the 1995 Kobe earthquake area: Comparison of finite-frequency and ray approaches. *Geophysical Journal International*, *187*(1), 278–302. https://doi.org/10.1111/j.1365-246X.2011.05139.x

VanDecar, J., & Crosson, R. (1990). Determination of teleseismic relative phase arrival times using multi-channel cross-correlation and least squares. *Bulletin of the Seismological Society of America*, *80*(1), 150–169. https://doi.org/10.1785/BSSA0800010150

van Herwaarden, D.-P., Thrastarson, S., Hapla, V., Afanasiev, M., Trampert, J., & Fichtner, A. (2023). Full-waveform tomography of the African Plate using dynamic mini-batches. *Journal of Geophysical Research: Solid Earth*, *128*(6), e2022JB026023. https://doi.org/10.1029/2022JB026023

Wang, K., Wang, Y., Song, X., Tong, P., Liu, Q., & Yang, Y. (2022). Full-waveform inversion of high-frequency teleseismic body waves based on multiple plane-wave incidence: Methods and practical applications. *Bulletin of the Seismological Society of America*, *112*(1), 118–132. https://doi.org/10.1785/0120210094

Weidle, C., Agard, P., Meier, T., Ducassou, C., & El-Hussain, I. (2013). *Cool (crust of the Oman ophiolite and its lithosphere) seismic network*. GEOFON Data Archive. https://doi.org/10.7914/SN/5H_2013

Weidle, C., Glück, E., Deif, A., El-Hussain, I., & Meier, T. (2025). Seismicity and state of stress in NE Arabia. *Geological Society, London, Special Publications*, *550*(1), SP550–2023. https://doi.org/10.1144/SP550-2023-214

Weidle, C., Wiesenberg, L., El-Sharkawy, A., Krüger, F., Scharf, A., Agard, P., & Meier, T. (2022). A 3-D crustal shear wave velocity model and Moho map below the Semail Ophiolite, eastern Arabia. *Geophysical Journal International*, *231*(2), 817–834. https://doi.org/10.1093/gji/ggac223

Weidle, C., Wiesenberg, L., Scharf, A., Agard, P., El-Sharkawy, A., Krüger, F., & Meier, T. (2023). Lithospheric evolution of eastern Arabia based on surface wave and receiver function analyses. *Earth and Planetary Science Letters*, *611*, 118145. https://doi.org/10.1016/j.epsl.2023.118145

Wiesenberg, L., Weidle, C., El-Sharkawy, A., Timkó, M., Lebedev, S., & Meier, T. (2022). Measuring the phase of ambient noise cross correlations: Anisotropic Rayleigh and Love wave tomography across the Oman Mountains. *Geophysical Journal International*, *231*(2), 1233–1251. https://doi.org/10.1093/gji/ggac232

Xi, J., Yu, Y., Zhao, D., & Hu, J. (2024). Modification of Archean cratons in southern Africa with foundered segments dropped into the shallow lower mantle. *Geology*, *52*(6), 468–472. https://doi.org/10.1130/G52023.1

Xu, P., & Zhao, D. (2009). Upper-mantle velocity structure beneath the North China Craton: Implications for lithospheric thinning. *Geophysical Journal International*, *177*(3), 1279–1283. https://doi.org/10.1111/j.1365-246X.2009.04120.x

Yamato, P., Agard, P., Goffé, B., De Andrade, V., Vidal, O., & Jolivet, L. (2007). New, high-precision P–T estimates for Oman blueschists: Implications for obduction, nappe stacking and exhumation processes. *Journal of Metamorphic Geology*, *25*(6), 657–682. https://doi.org/10.1111/j.1525-1314.2007.00722.x

Zhang, J., Dong, L., Wang, J., Wang, J., Wang, Y., & Huang, C. (2024). Eikonal-equation-based characteristic reflection traveltime tomography. *Geophysics*, *89*(1), U17–U30. https://doi.org/10.1190/geo2023-0326.1

Zhao, D., Hasegawa, A., & Kanamori, H. (1994). Deep structure of Japan subduction zone as derived from local, regional, and teleseismic events. *Journal of Geophysical Research*, *99*(B11), 22313–22329. https://doi.org/10.1029/94JB01149

Zhou, X., Lan, H., Chen, L., Guo, G., Lei, Y., Waheed, U. B., & Pan, S. (2021). An iterative factored topography-dependent eikonal solver for anisotropic media. *Geophysics*, *86*(5), U121–U134. https://doi.org/10.1190/geo2020-0662.1

Zhou, X., Lan, H., Chen, L., Guo, G., Waheed, U. B., & Badal, J. (2023). A topography-dependent eikonal solver for accurate and efficient computation of traveltimes and their derivatives in 3D heterogeneous media. *Geophysics*, *88*(2), U17–U29. https://doi.org/10.1190/geo2021-0799.1

Zhu, H., Yang, J., & Li, X. (2020). Azimuthal anisotropy of the North American upper mantle based on full waveform inversion. *Journal of Geophysical Research: Solid Earth*, *125*(2), e2019JB018432. https://doi.org/10.1029/2019JB018432